PNAS
www.pnas.org

Supplementary Information for

Bulk vs Layer Confined $RNiO_3$: Disentangling Lattice and Electronic Contributions to the Metal-Insulator Transition

Alexandru B. Georgescu, Oleg E. Peil, Ankit S. Disa, Antoine Georges,Andrew J. Millis

Alexandru B. Georgescu.
E-mail: ageorgescu@flatironinstitute.org

This PDF file includes:

Supplementary text
Figs. S1 to S11
References for SI reference citations

Supporting Information Text

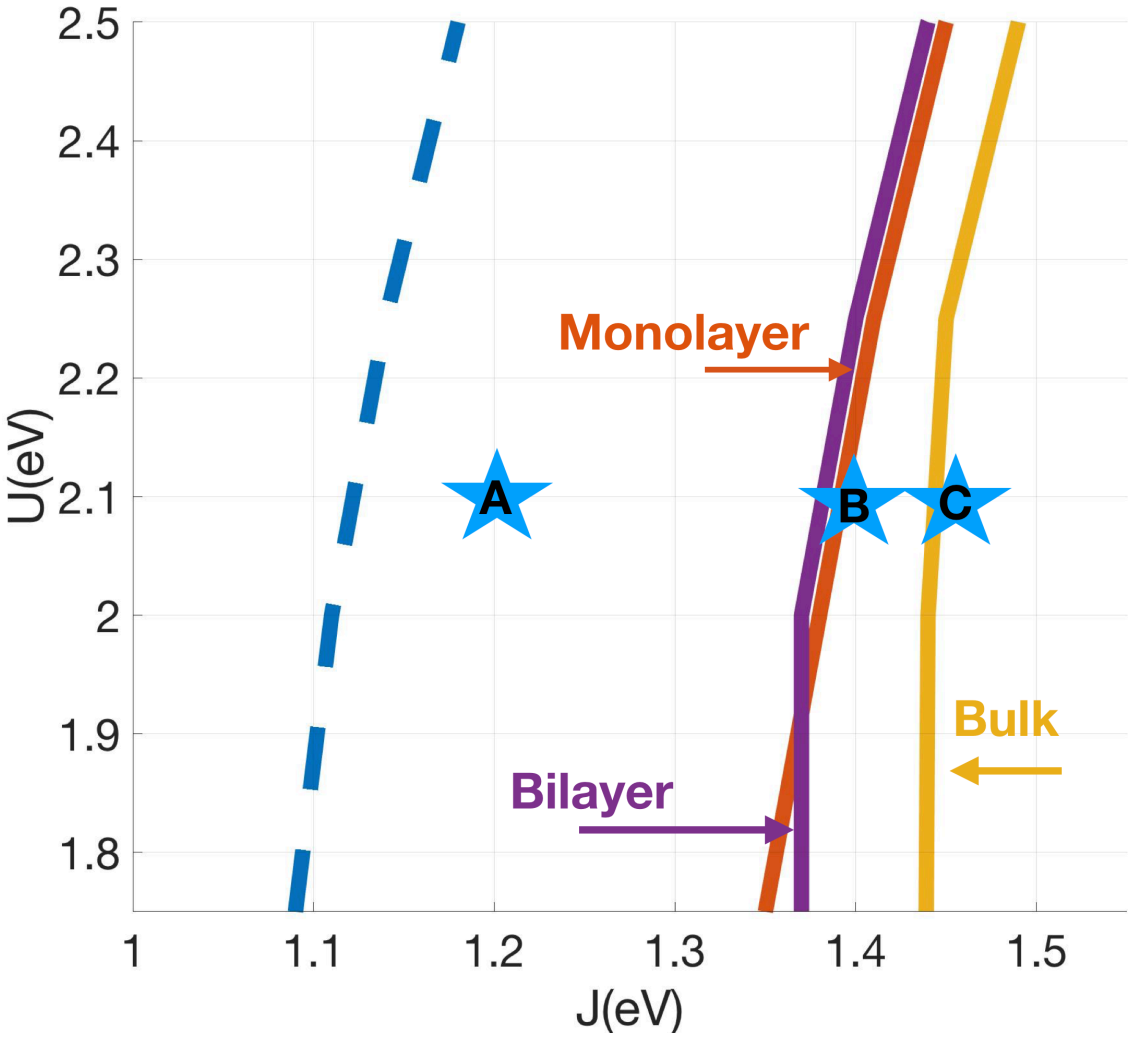

Fig. S1. Solid lines: boundaries of region of spontaneous electronic disproportionation and the associated metal-insulator transition in the (U,J) plane for DFT-relaxed bulk, bilayer and monolayer NNO in the absence of structural distortion. Insulating phases are to the right of the lines shown. The dotted line to the left shows the Metal-Insulator transition line for the bulk experimental Low T disproportionated structure calculated as in Ref (1). The phase diagram shows the same trend as the contructions in the main text, with the bulk less prone to electronic disproportionation than the heterostructures. The stars correspond to the points at which the constructions in the main text are plotted.

Appendix A: DFT+DMFT Q=0 Phase Diagram. In Figure S1 we plot the metal-insulator phase diagram calculated at $Q = 0$ for the different materials on the plane of interaction parameters U and J. , i.e. determined by $E_{el}(\Delta N)$ exclusively. We also plot a dashed line corresponding to the MIT transition for the experimental bulk low temperature, insulating structure, calculated as in Ref. (1), to show the effect of the lattice distortion. We choose parameters U,J in the range in which the bulk undisproportionated material is metallic. We note that the resulting J needed to obtain an insulating state is significantly higher than in a more realistic calculation involving U,J and an inter-site Hartree term V(2), however for simplicity and to avoid overfitting multiple parameters we work within a U, J model as in previous work (1). Consistent with previous work we find insulating solutions for values U,J that are to the right of U-3J<0 (which corresponds to spontaneous electronic disproportionation in the atomic limit), insulating solutions, in the absence of any structural disproportionation. The transitions as a function of U and J are strongly first order. We find that spontaneous disproportionation ($\Delta N \neq 0$) is achieved for a slightly smaller critical J for a given U in the monolayer and the bilayer than in the bulk. Despite minor differences in bandwidth, the phase diagrams for the monolayer and bilayer are nearly identical.

Appendix B: DFT Technical Details

We use the Quantum Espresso (3) software package for our DFT calculations, Wannier90(4) to generate the extended Wannier e_g orbitals, and the TRIQS software package(5) for the DMFT calculations with its various applications: DFTTools (6) for the interface with Wannier90 and the CT-HYB DMFT solver(7) to solve the DMFT equations using the Hybridization expansion impurity solver (8). We use ultrasoft pseudopotentials (9) and the PBE (10) version of the GGA exchange-correlation functional formalism. To simulate the bulk material, we used a 20 atom c(2x2)x2 unit cell, relaxed starting from the experimental structure; for the m=1 superlattice we used 1 layer of NNO and 3 layers of NAO, while for m=2 we used 2 layers of each material, making sure that the total number of layers is even in order to allow the octahedra to relax. For the bulk undisproportionated calculation, we find that our high-temperature relaxed structure within GGA has a bandwidth that is only slightly smaller than the experimental high temperature structure. In the phase diagram in figure 2, this leads to a small shift to the left in the critical J for a given U of at most 0.05eV. Of the available functionals we have tried however (LDA, PBE and PBEsol), we find that relaxations using GGA in the PBE formalism provide a bandwidth that is very close to the one using the experimental high temperature structure as well as a phase diagram that is closer to the one obtained by using said structure. We also find that the phase diagram difference between the undisproportionated structures is robust with respect to changing the functional used in order to obtain the relaxed structures. For the initial DFT relaxations without structural disproportionation, we found a k-point mesh of 5x5x4 for the 20 atom bulk unit cell or 5x5x4 for the heterostructures (equivalent to 7x7x8 and 7x7x12) per formula unit are sufficient to generate quality structures. For consistency with the DFT+U results, we also performed higher k-point calculations but found they do not affect results. For the various DFT+U relaxations involving structural disproportionation, we impose ferromagnetic order. The k-point mesh has to be higher to differentiate between the various possible local minima. Thus, for the 20 atom bulk is 7x7x5, while for the 40 atom heterostructures it is 7x7x4 (roughly equivalent to a 10x10x10 k-mesh per formula unit) in order to have a 1meV accuracy in the total energies of the relaxed structures, however we have found that structures obtained using 5x5x2 and 7x7x3 k-point grids give nearly identical structural results. For all calculations, the wavefunction energy cutoff is 35 Ry, and the density cutoff is 280Ry. A Marzari-Vanderbilt smearing of 0.027 eV is used for the electron occupation function for all calculations. The energy convergence threshold for relaxations is 10^{-9}eV and the force covergence threshold is $10^{-4} a.u.$, the electronic energy convergence threshold within the electronic self-consistency loop is 10^{-12}eV.

To extract the tight-binding parameters for DMFT calculations, we obtain the antibonding e_g orbitals as a postprocessing step using Wannier90 within the Maximally Localized Wannier Function framework.

Appendix C: DFT+U Results and Technical Details. One of the more difficult aspects of our calculations was obtaining structurally disproportionated states for the heterostructures. While for the bulk material one can start from the experimental, low-temperature insulating structure and perform a DFT+U, ferromagnetically ordered calculation, it is not trivial to obtain structurally disproportonated solutions for the heterostructures. In order to obtain said solutions we first performed non-magnetic, DFT calculations to obtain a starting, metallic, non-disproportionated solution. We then manually moved the Oxygen atoms of the resulting NiO_6 octahedra closer or further away from the Ni atoms in an alternating way, and relaxed the structure imposing a starting ferromagnetic electronic order and a U=4eV. Following this relaxation we used the resulting structure as an input to other relaxations with lower and larger U to obtain a set of structures with smoothly varying parameters. For very small U (U=0ev-1eV) it is more difficult to obtain structures that are part of a continuous set of structures, so we excluded the structures at U=1eV that are not part of the set.

For the DFT+U calculations, we performed calculations in the ferromagnetic phase, as our unit cells are not large enough to reproduce the full experimentally determined magnetic structure in the bulk (with vector q=(1/4,1/4,1/4)) or bilayer (q=(1/4,1/4,0) while the magnetic structure in the monolayer is not known but with ferromagnetism and a q=(1/4,1/4,0) vector excluded. We use the FM state as a way to break symmetry leading to bond disproportionation and an alternating S=1, S=0 state, as more important in the physics of the final structure than the exact magnetic order. A Hund J is included implicitly within spin-polarized DFT, however within the version of Quantum Espresso used for these calculations, only the effective Dudarev $U_{eff} = (U - 2J)$ scheme is available, not allowing us to control U, J separately. For the two inequivalent Ni sites, as a proxy for charge disproportionation, we use the difference in local magnetic moment. We find that the total magnetization for the supercell is always equal to one Bohr magneton times the number of Nickel sites, as we would expect. However, the

projected magnetic moment on the Löwdin orbitals does not add up to this total magnetization, as the Löwdin orbitals are not sufficient to describe the e_g valence states. However, making the assumption that the Löwdin magnetic moment is directly proportional to the magnetic moment per site, we can then write $m_{Ni} \approx m_{Lowdin-total} * 2\mu B/m_{total}$ where $m_{Lowdin-total}$ is the total magnetization per pair of Ni sites: this is the ΔM.

Further supporting the picture of stronger electronic disproportionation in the heterostructures as a driving mechanism, we present results for the bulk, bilayer and monolayer structures as obtained by DFT+U using spin-polarized calculations in the FM state and full relaxations in Figure S2. We find that, for small U (U=0ev,1eV), the heterostructures have a critical U under which the lattice stiffness is too strong to allow disproportionation, and even when it is allowed, there is a competition between the disproportionated state and a Jahn-Teller distorted state with lower disproportionation. As expected, the critical U at which the monolayer disproportionates is higher than for the bilayer which is higher than for the bulk. Consistent with the DFT+DMFT results, however, once electronic disproportionation is allowed the monolayer is more electronically disproportionated than the bulk. Q are very similar for all three structures, with the exception of large U for which both the bulk and bilayer structural disproportionation stop increasing, while the monolayer disproportionation increases past that of both.

We also present structural information on the structures obtained for various U within DFT+U and note which structures were excluded from our fit for the various parameters in Figures S3, S4 and S5

Appendix D: DFT+DMFT Technical Details. The Slater-Kanamori Hamiltonian solved by DMFT using the tight binding model extracted from the Wannier functions has the form on each lattice site:

$$\hat{H}_U = U \sum_m \hat{n}_{m\uparrow}\hat{n}_{m\downarrow} + (U-2J) \sum_{m\neq m'} \hat{n}_{m\uparrow}\hat{n}_{m'\downarrow} + (U-3J) \sum_{m<m',\sigma} \hat{n}_{m\sigma}\hat{n}_{m'\sigma} - J \sum_{m\neq m'} c^\dagger_{m\uparrow} c_{m\downarrow} c^\dagger_{m'\downarrow} c_{m'\uparrow} + J \sum_{m\neq m'} c^\dagger{}_{m\uparrow} c^\dagger_{m\downarrow} c_{m'\downarrow} c_{m'\uparrow} \quad [1]$$

In the DFTTools interface between DFT and DMFT we use a k-mesh of 14x14x14 for the bulk material, and a k-mesh of 12x12x6 for the heterostructure to obtain quality local density of states. The DMFT calculations in this paper are performed in a single-shot formalism, i.e. the new density is not updated into the DFT loop. Most DMFT calculations in this paper, unless mentioned otherwise, are done at an inverse temperature $\beta = 40eV^{-1}$, equivalent to a temperature of 290K. Most DMFT calculations are run for 15 steps using 10^7 QMC cycles. Calculations that require higher precision are ran for 35 steps, the first 30 using around 10^7 QMC cycles, and the final 5 using 3×10^8 cycles. To compare with previous literature, we've also performed density-density only calculations to benchmark our calculations. We find that using the Slater-Kanamori Hamiltonian shifts the metal-insulator phase boundary to slightly higher values of J given a particular U ($\approx 0.2eV$).

Appendix E: Model Parameter Extraction. In order to extract the relevant parameters we need, we use the structures generated within DFT+U, carefully selecting them such that a smooth variation of the structural parameters is obtained as described in Appendix D. We need to extract the following: $g^{DFT} = \frac{\partial \Delta_S}{\partial Q}$, $\chi_0 = \frac{\partial \Delta N}{\partial \Delta_S}$, $\lambda = g^{DFT}\chi_0$ and finally the stiffness k, which can then be extracted by doing DFT calculations on said structures. We then get: $E_{DFT}(Q) = (\frac{k}{2} - \frac{1}{4}(g^{DFT})^2\chi_0)Q^2 = \frac{c}{2}Q^2$ with c, g, χ_0 constants we extract from the structures we generated as a function of Q. Our results are shown in Figures: S6, S7, S8 and S9. In order to benchmark this method as compared to explicitly imposing a Q, we compared our results on the bulk material with previous work (11) in which multiple structures were generated by modulating the bond disproportionation Q alone, and find that our results are consistent. We also note that while using bulk structures obtained through GGA relaxation does lead to slightly lower bandwidths than those obtained using the experimental structure, this only affects the results by shifting all the phase diagrams to lower J for a given U by about $0.05eV$ as compared to the experimental structure. As the stiffness k and the static response functions $g^{DFT} = \frac{\partial \Delta_S^{DFT}}{\partial Q}$ and $\chi_0 = \frac{\partial \Delta N^{DFT}}{\partial \Delta_S^{DFT}}$ do not depend on the bandwidth by more than a fraction of a percent within our calculations, and the bond angles of the disproportionated structures remains the same up to within < 1 degree within our relaxed spin-polarized calculations, we can simulate a large number of disproportionated structures with varying Q and assuming that the DFT Hamiltonian would look like the one corresponding to the undisproportionated, nonmagnetic structure plus an on-site energy difference $\Delta_S^{DFT} = g^{DFT}Q$. The spin-polarized relaxed structures have bond angles that are slightly more bent than those in the non-magnetic calculations, however as was shown in (11), neither k nor g depend on the bandwidth; we do expect a slightly larger χ_0 in the structures obtained using spin-polarized DFT+U by about 3-5% due to the slightly reduced bandwidth.

Appendix F: Experimental Hole Determination. Experimental values of the Ni eg hole ratio were extracted from x-ray linear dichroism (XLD) measurements on NNO/NAO superlattices, which can be directly compared to theory. The sample growth and measurement procedures are described in Ref. (12). To extract r experimentally, the XLD sum rule (13) is applied for the Ni L edge, $r=\frac{3I_{3z^2-r^2}}{4I_{x^2-y^2}-I_{3z^2-r^2}}$, where Ip corresponds to the integrated absorption measured with the polarization parallel to p. Figure S10 shows the absorption for in-plane and out-of-plane polarizations as well as the difference spectrum of the monolayer NNO/NAO superlattice. The values of r for the monolayer NNO/NAO superlattice, bilayer NNO/NAO superlattice, and bulk NNO samples are 0.91 ± 0.03, 1.00 ± 0.02, and 1.02 ± 0.02, respectively.

Appendix G: DFT+U Structures. One of the most difficult aspects of our calculation consisted in obtaining disproportionated structures for the heterostructures using DFT+U. To best serve future research in this direction, we present the lattice vectors and atomic coordinates obtained within DFT+U for the bulk, $(NNO)_2/(NAO)_2$ and $(NNO)_1/(NAO)_3$ structures for U=4 using PBE as the exchange correlation potential and ultrasoft pseudopotentials. To obtain undisproportionated (Q=0) structures, one can use these structures as input for a DFT calculation without U and without magnetism. To obtain structures with varying amounts of disproportionation Q as in Appendix E, one can perform calculations with Ferromagnetic order with slowly increasing/decreasing U in order to obtain structures with varying Q but similar Jahn-Teller distortion. The in-plane lattice constant of the heterostructures is fixed to the DFT values of the in-plane lattice constant of NNO in order to avoid issues related to the separate relaxation of the unit cell of NAO.

Estimation of Q and Relative Oxygen Displacements Each octahedron has two inequivalent bond lengths in the xy plane; the bond lengths along z are equivalent for the monolayer and the bulk but not for the bilayer. To obtain Q, we take differences of pairs of bond lengths corresponding to the two inequivalent octahedra as follows: we pick the longer in-plane Ni-O bonds for each an take the difference between the large and small octahedron, then the difference between the shorter in-plane Ni-O bonds, and finally the equivalent out-of-plane Ni-O bonds. We then have Q as mentioned in the main text:

$$Q = \sqrt{\frac{\sum_i (l_{LB}^{(i)} - l_{SB}^{(i)})^2}{6}} \qquad [2]$$

where $l^{(i)}$ are the lengths of the Ni-O bonds. In order to estimate the relative oxygen displacements along the Ni-Ni lines as shown in Figure 2 in a consistent manner (avoiding issues related to the Jahn-Teller distortions) we had to use certain approximations. Namely, for the in-plane average displacement, we take the difference between the average in-plane bond length of each octahedra and multiply it by $\cos((\bar{\angle}_{O-Ni-Ni}))$, where $\bar{\angle}_{O-Ni-Ni}$ corresponds to averaging over the O-Ni-Ni bond angle. For the out-of-plane displacement of the oxygen atoms atoms along the Ni-Ni direction, we perform the same calculation but without averaging over bond angles. We note that this gives the same result as calculating the displacement along z. For the Ni-O-Al displacement, as the interfacial disproportionation mode involves additional complications (relative displacements along z of the two Al atoms and a slight displacement along x-y relative to the Ni atoms), we take the relative displacement of the atoms along z instead as the Al atoms are slightly displaced along z relative to each other and along the xy plane relative to Ni.

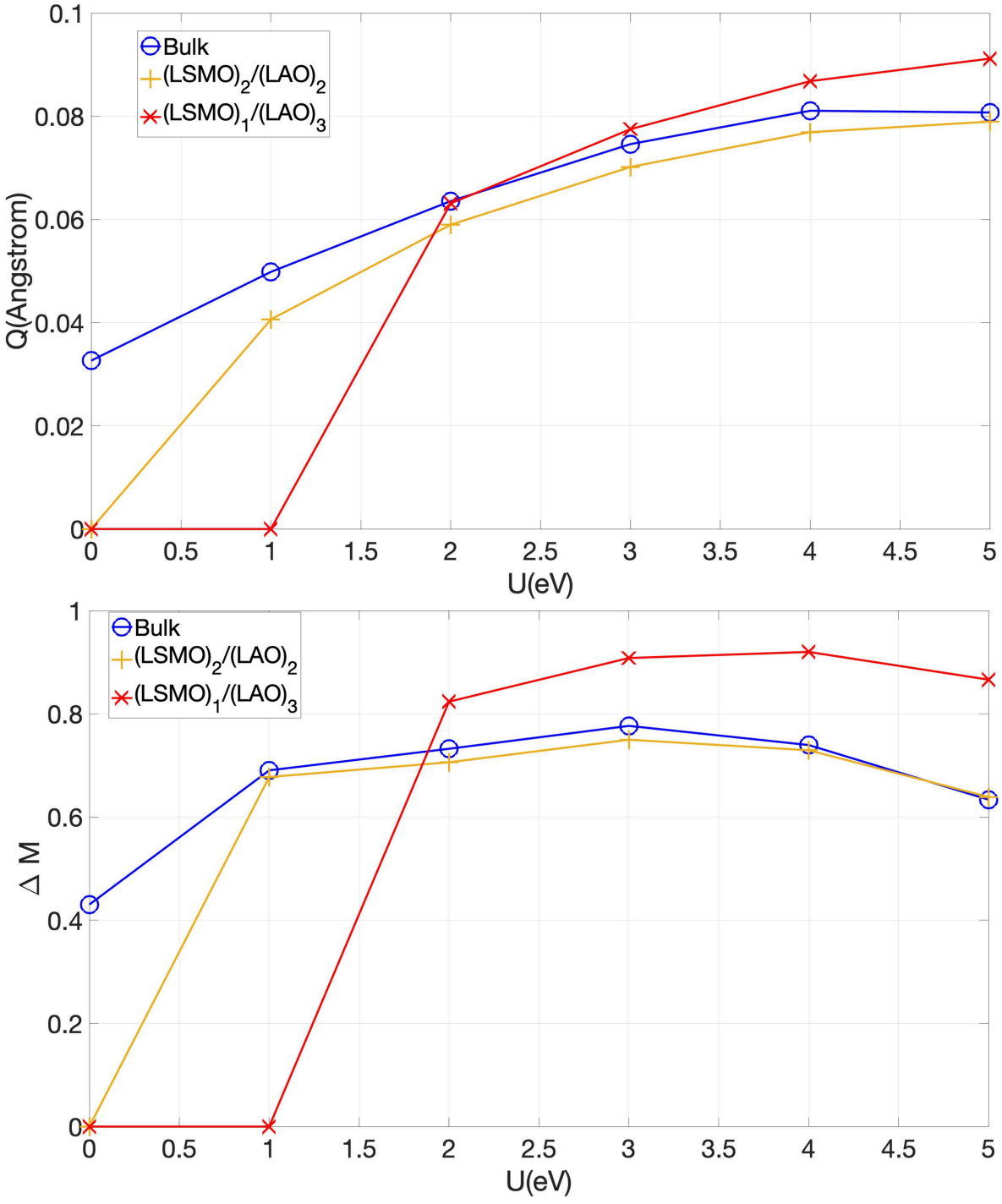

Fig. S2. Electronic and structural disproportionation within DFT+U for the various relaxed structures. For small U=0eV for all structures as well as for U=1eV for the heterostructures we picked the local minimum corresponding to a similar symmetry as for the higher U.

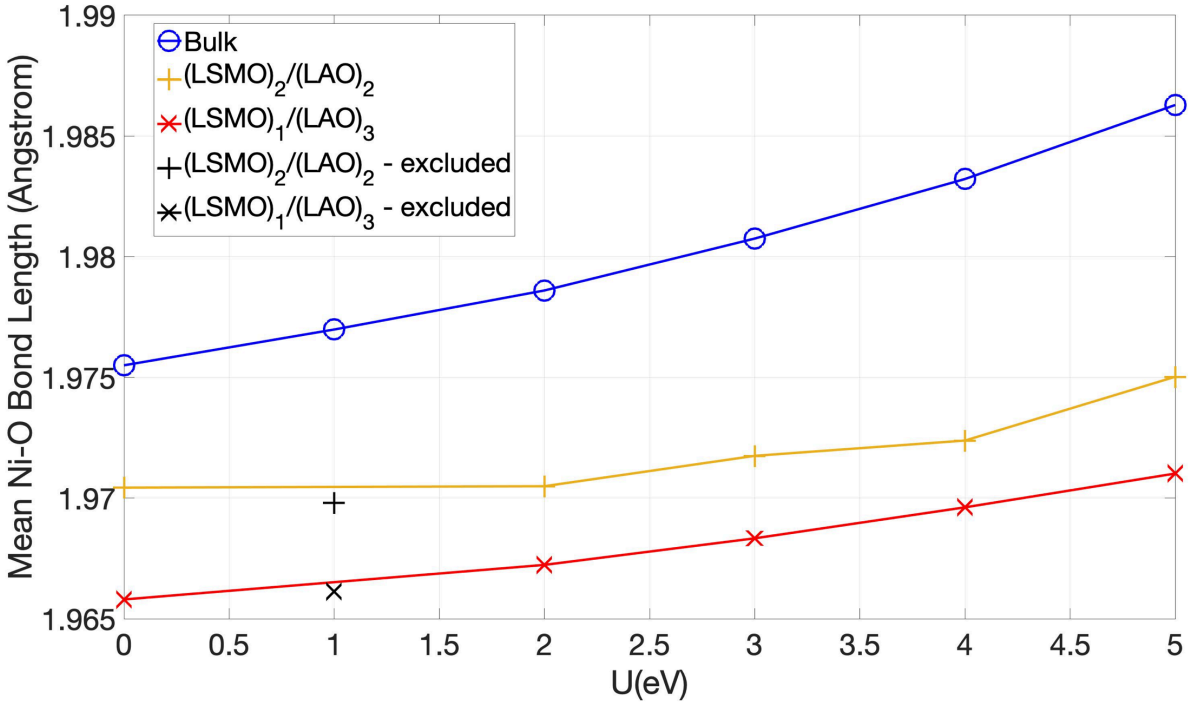

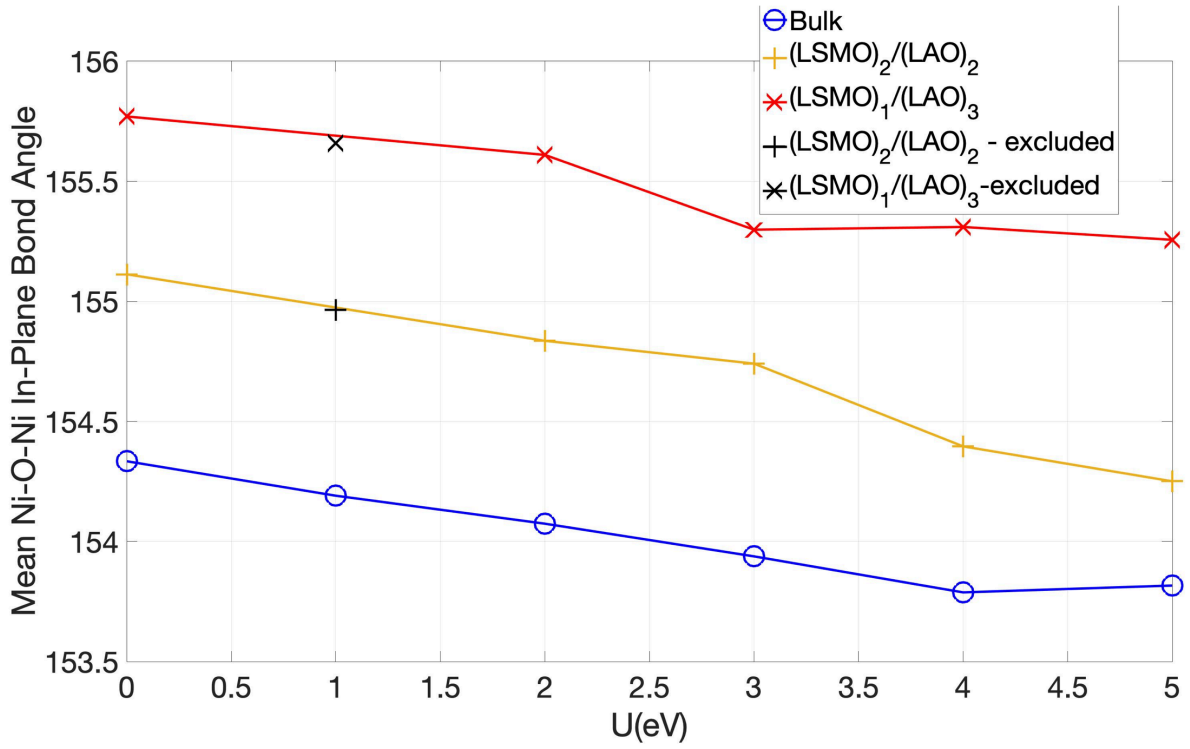

Fig. S3. Mean Ni-O bond lengths and mean in plane Ni-O-Ni bond angles for the structures used to obtain the parameters for our model as a function of the U used to generate the heterostructures. For U=0eV we picked the local minimum corresponding to the same symmetry as for the higher U. For the heterostructures at U=1eV we did not obtain a structure that continuously fits among the others and did not use it for the fit. We include all points for reference.

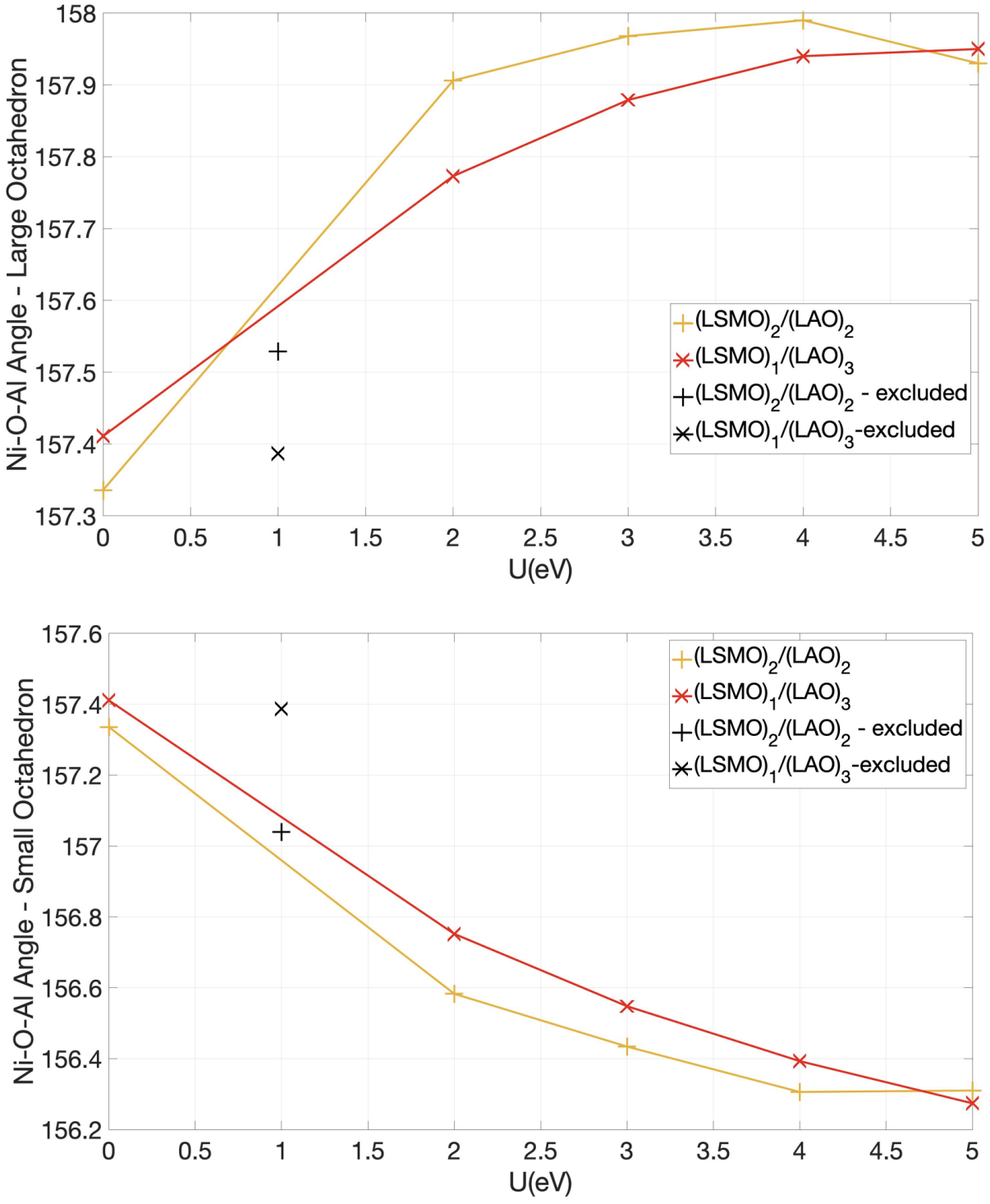

Fig. S4. Ni-O-Al bond angles for the large and small NiO_6 octahedra. The bond angles corresponding to the larger octahedra are straighter. Plot is as a function of the U used to generate the structures within DFT+U. For U=0eV we picked the local minimum corresponding to the same symmetry as for the higher U. At U=1eV we could not obtain a structure that continuously fits among the others and did not use it. We include the resulting points for reference.

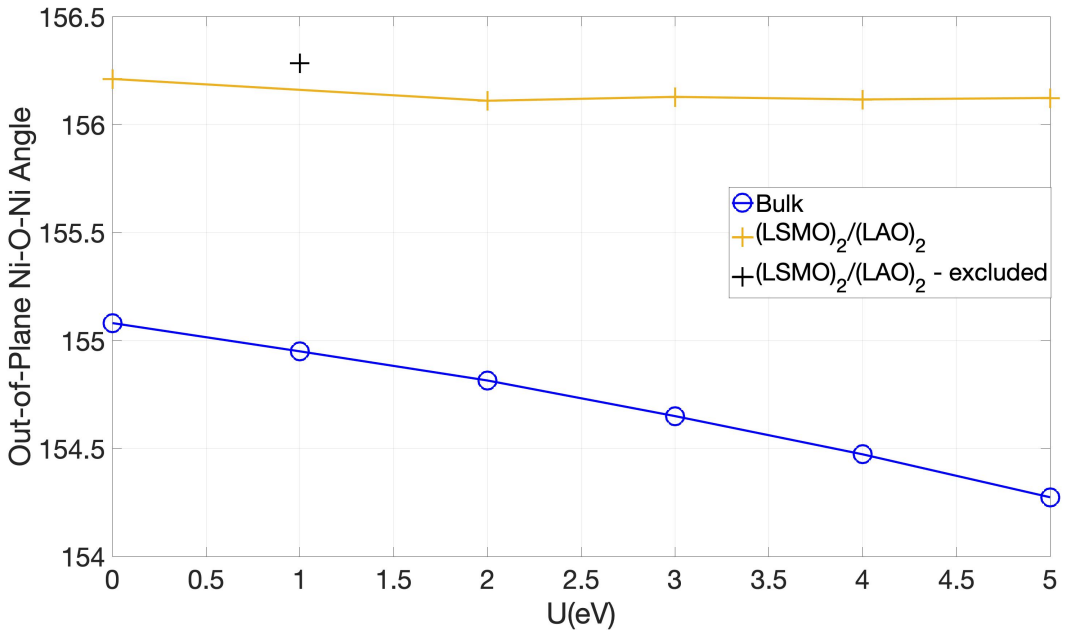

Fig. S5. Ni-O-Ni out of plane angles. Plot is as a function of the U used to generate the structures within DFT+U. For U=0eV we picked the local minimum corresponding to the same symmetry as for the higher U. At U=1eV for the bilayer we could not obtain a structure that continuously fits among the others and did not use it. We include the resulting points for reference.

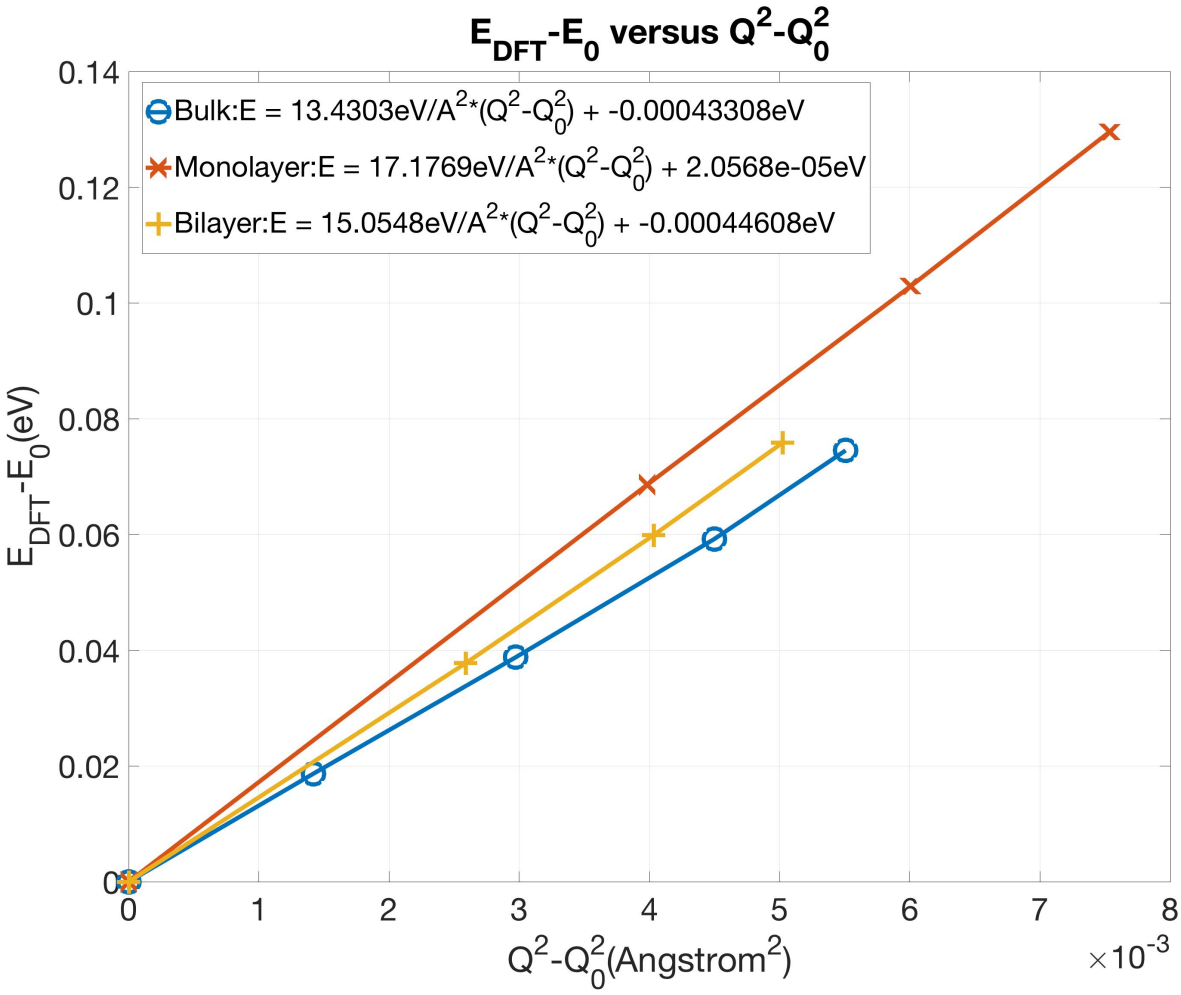

Fig. S6. Plot of energy per 2 formula units of NNO for the different structures for different Q, using structures obtained from DFT+U calculations. The energy and Q^2 are plotted relative to the energy of the smallest Q that are included in the plot.

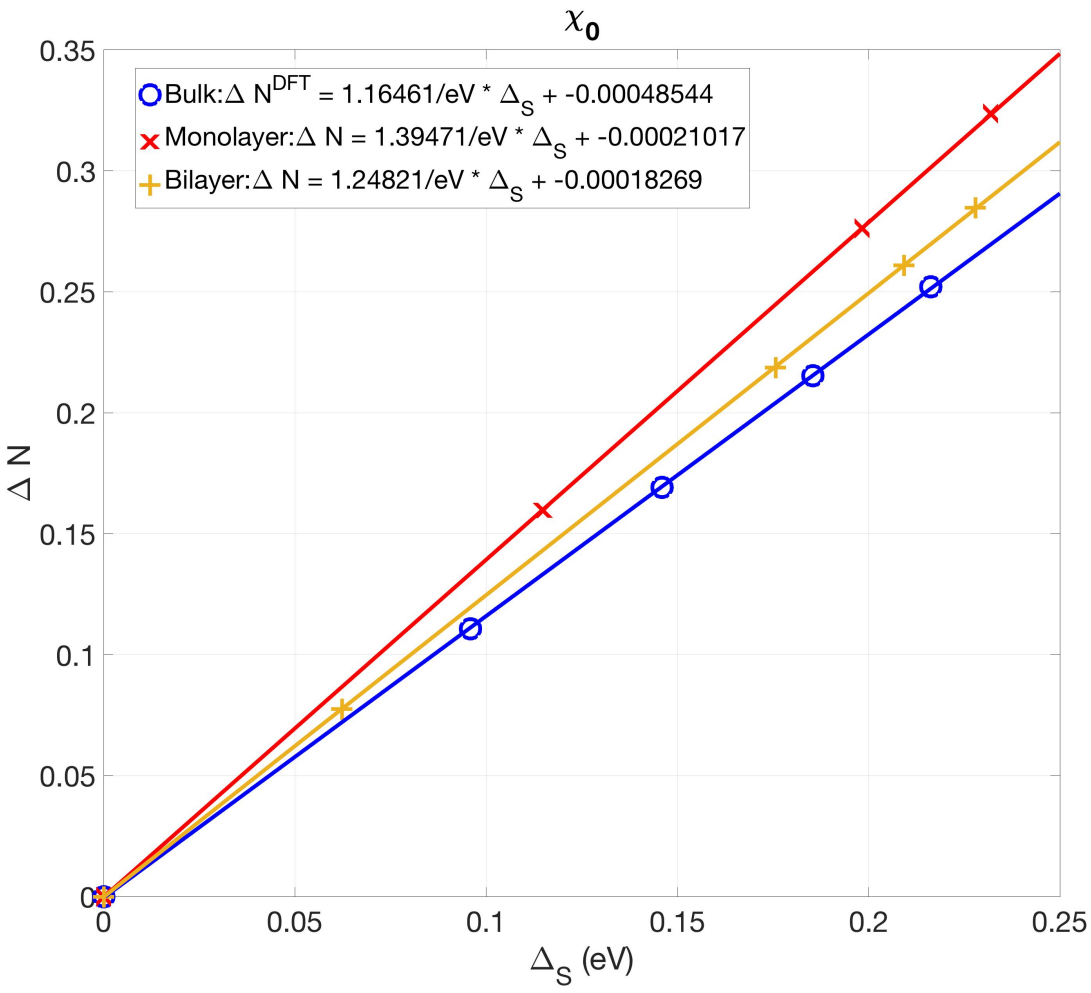

Fig. S7. Fit to obtain the static electronic response for the three materials, χ_0

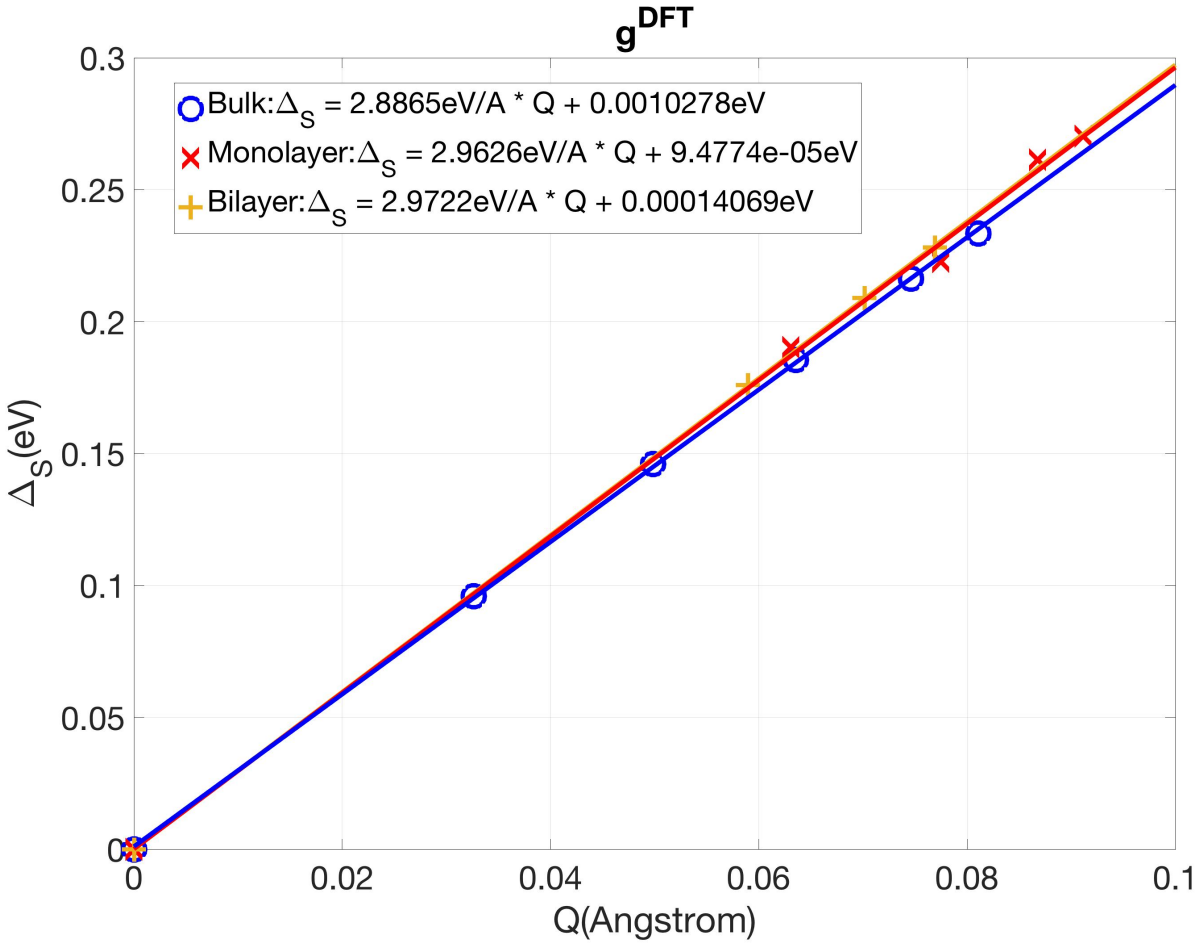

Fig. S8. Fit to obtain the linear coupling coefficient within DFT, g^{DFT}

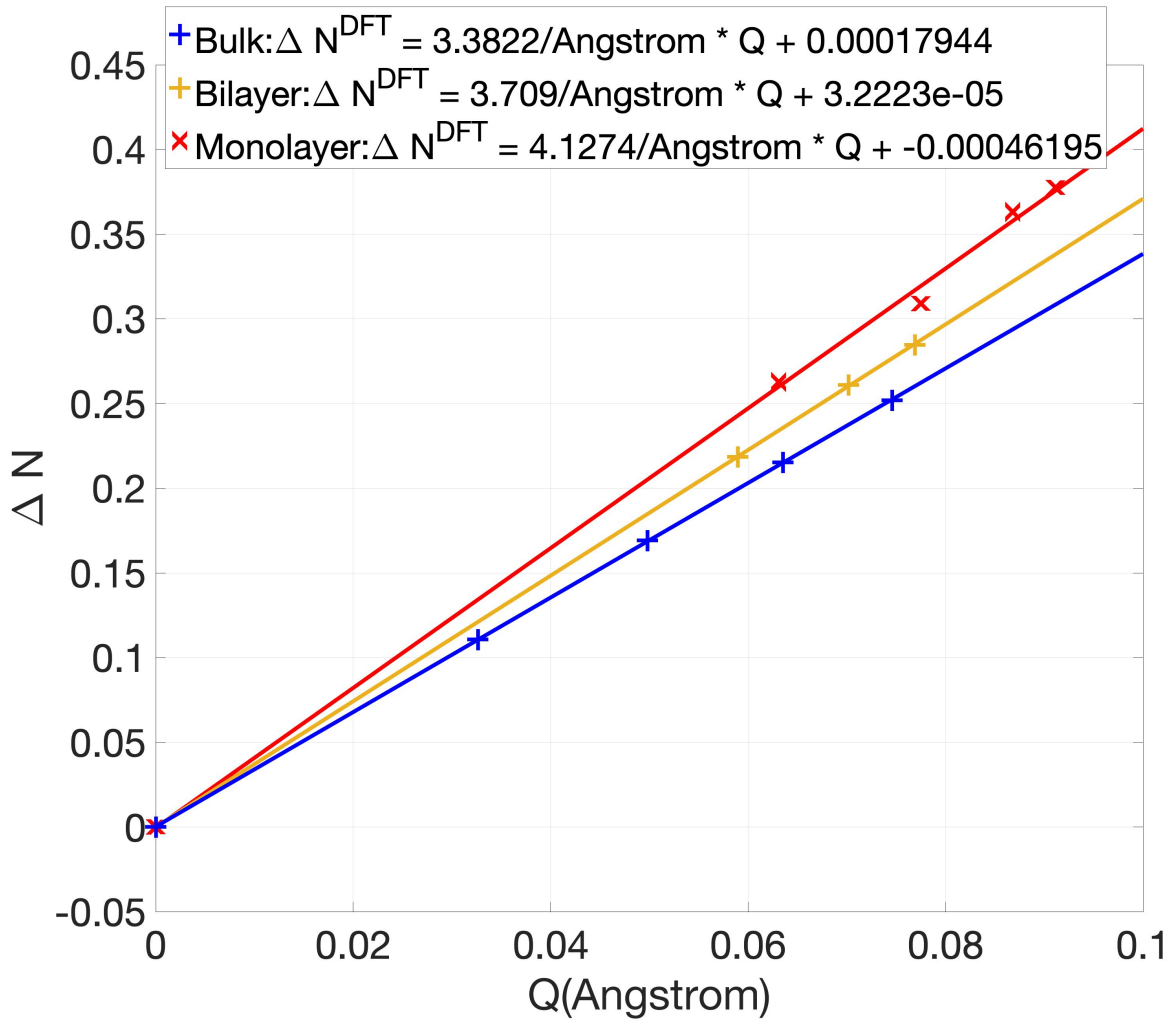

Fig. S9. ΔN^{DFT} versus Q as extracted from DFT; $\frac{\Delta N}{Q} = \lambda^{DFT} = g^{DFT}\chi_0$ as obtained from this fit compares well with the results from multiplying the previously obtained $g^{DFT}\chi_0$

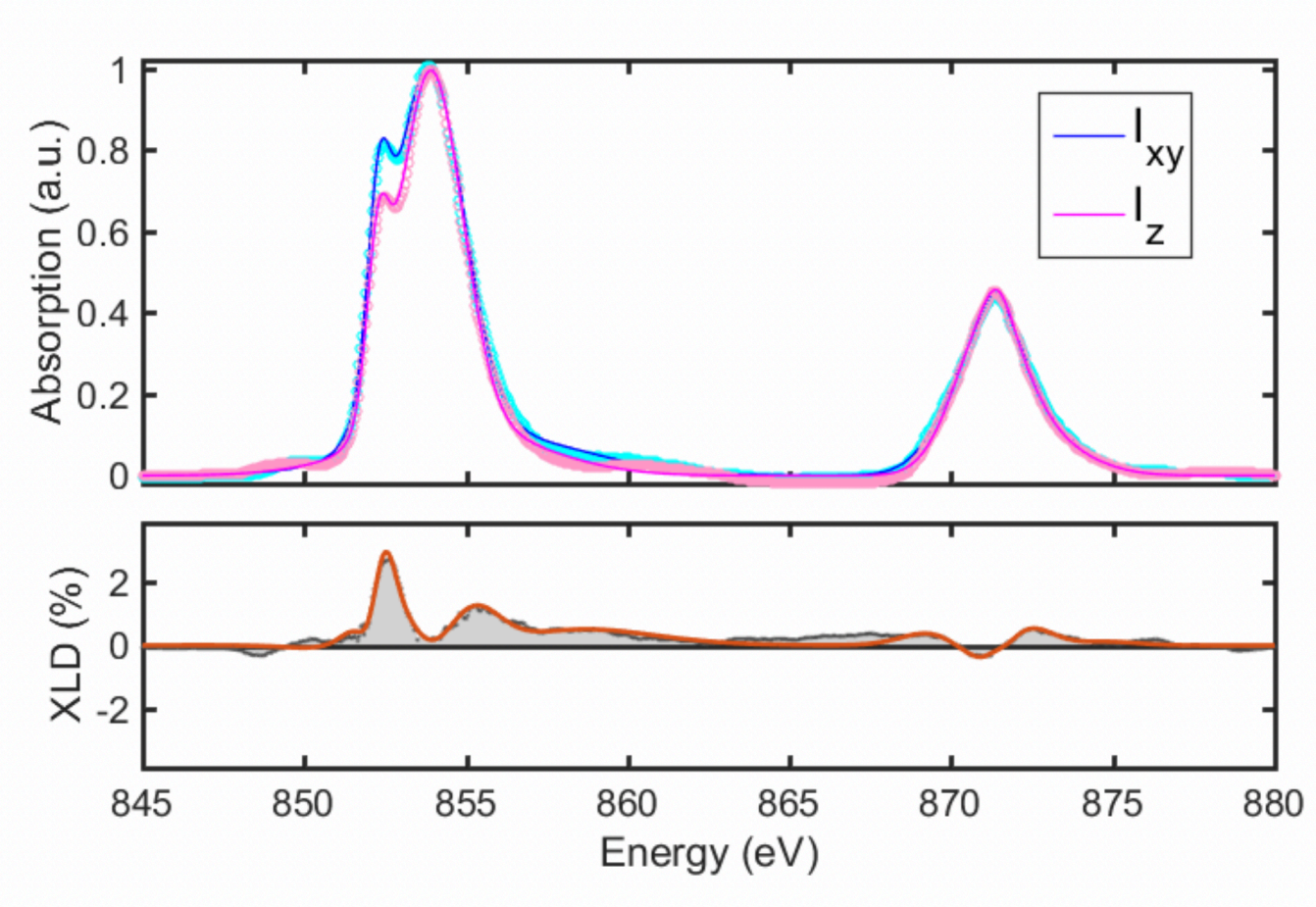

Fig. S10. (top) X-ray absorption spectra and (bottom) x-ray linear dichroism of monolayer NNO/NAO superlattice. Blue and pink curves in top panel correspond to absorption with polarization in-plane and out-of-plane, respectively.

$(NNO)_1/(NAO)_3$

Cell Parameters (in Angstrom):
v1=(5.409, 0.0, 0.0)
v2=(0.0, 5.4611, 0.0)
v3=(0.0, 0.0, 15.175280)

Atomic positions (in crystal coordinates):

Al	0.002291200	0.504226268	0.870278522
Al	0.499365893	0.004510625	0.871532046
O	0.272860482	0.279302045	0.888698314
O	0.773709122	0.231657323	0.854909303
O	0.224525821	0.777699894	0.888404474
O	0.729333362	0.728528955	0.854353892
Nd	-0.004972271	-0.023052494	0.747584510
Nd	0.507235555	0.476933097	0.747419071
O	0.064305399	0.509316644	0.747045799
O	0.438756953	0.009983690	0.747854337
Al	0.001090974	0.498002330	0.623338698
Al	0.501095952	-0.001998455	0.623342159
O	0.267806573	0.264662436	0.606676326
O	0.767541455	0.230816295	0.639861802
O	0.234632427	0.765210494	0.606820881
O	0.734374530	0.731356814	0.640002390
Nd	0.007165467	0.019092677	0.499077428
Nd	0.494936041	0.519118225	0.499234985
O	-0.062103468	0.486713918	0.499618681
O	0.563415880	-0.013967416	0.498815709
Al	-0.000113376	0.491832442	0.376357309
Al	0.502826771	-0.008443170	0.375118034
O	0.272846493	0.267513534	0.392296392
O	0.777654542	0.218342335	0.358257758
O	0.228474912	0.764388246	0.391739703
O	0.729306855	0.716740686	0.357966131
Nd	-0.002865895	-0.041861737	0.248534583
Nd	0.512079113	0.455946706	0.248640397
O	0.073676124	0.506938202	0.248813517
O	0.434338692	0.007096125	0.253172304
Ni	0.001080198	0.498058289	0.123307519
Ni	0.501087166	-0.001965303	0.123310511
O	0.280551672	0.290699118	0.102781221
O	0.206911829	0.779326018	0.102977656
O	0.795245358	0.216799581	0.143667880
O	0.721635647	0.705427054	0.143865883
Nd	0.005040367	0.037946435	-0.001889267
Nd	0.490083803	0.540133267	-0.002001036
O	-0.071531151	0.489149511	-0.002178785
O	0.567826734	-0.011021368	-0.006534040

$(NNO)_2/(NAO)_2$

Cell Parameters (in Angstrom):
v1=(5.409, 0.0, 0.0)
v2=(0.0, 5.4611, 0.0)
v3=(0.0, 0.0, 15.288983)

Atomic positions (in crystal coordinates):

Al	0.002354058	0.507015921	0.871525770
Al	0.499916979	0.006858316	0.870690215
O	0.275415606	0.278821961	0.888677035
O	0.771640150	0.233407070	0.854447461
O	0.229802143	0.780067435	0.888692268
O	0.729509987	0.735484094	0.854758027
Nd	-0.006056450	-0.019276186	0.748142290
Nd	0.507206098	0.480722892	0.748499805
O	0.064015077	0.515509833	0.748811664
O	0.437133626	0.015514756	0.747836103
Al	0.001247649	0.506854806	0.625951477
Al	0.498801669	0.007011886	0.625121740
O	0.271369183	0.280077131	0.607965285
O	0.771654506	0.235470427	0.641870908
O	0.225728263	0.778832092	0.607981764
O	0.729501557	0.733389299	0.642185188
Nd	0.005419270	0.038437488	0.499427789
Nd	0.490137400	0.539614944	0.499663738
O	-0.072537841	0.488615537	0.500667844
O	0.567965132	-0.010145273	0.503477953
Ni	0.000413083	0.495084380	0.374942243
Ni	0.501681588	-0.005269661	0.375061871
O	0.282716972	0.288026372	0.395152629
O	0.796011931	0.209908246	0.353879001
O	0.206699657	0.778880710	0.395008325
O	0.716917277	0.700410390	0.353765243
Nd	-0.010195242	-0.053963199	0.248217546
Nd	0.511410483	0.446035929	0.248430179
O	0.075098545	0.503873635	0.251539015
O	0.426133591	0.003859997	0.245135490
Ni	-0.000487426	0.494725501	0.121615235
Ni	0.500783686	-0.004916256	0.121721417
O	0.294522169	0.278915625	0.101680597
O	0.218434375	0.788070787	0.101534093
O	0.784310194	0.200375998	0.142873773
O	0.705159603	0.709876499	0.142754624
Nd	0.011037976	0.039629123	-0.003007638
Nd	0.495745808	0.538451129	-0.002775951
O	-0.066792587	0.489865558	-0.006827409
O	0.573697455	-0.011376090	-0.004021607

(NNO)-bulk

Cell Parameters (in Angstrom):
v1=(5.421605612 0.000000000 -0.000867789)
v2=(0.000000000 5.534560397 0.000000000
v3=(-0.009805518 0.000000000 7.694108641)

Atomic positions (in crystal coordinates):

Nd	0.988403755	0.052409150	0.249942861
Nd	0.011596245	0.947590850	0.750057139
Nd	0.511596245	0.552409150	0.250057139
Nd	0.488403755	0.447590850	0.749942861
Ni	0.500000000	0.000000000	0.000000000
Ni	-0.000000000	0.500000000	0.500000000
Ni	0.500000000	0.000000000	0.500000000
Ni	-0.000000000	0.500000000	0.000000000
O	0.078881709	0.485104567	0.255315024
O	0.921118291	0.514895433	0.744684976
O	0.421118291	0.985104567	0.244684976
O	0.578881709	0.014895433	0.755315024
O	0.703751849	0.284852430	0.042686134
O	0.296248151	0.715147570	0.957313866
O	0.796248151	0.784852430	0.457313866
O	0.203751849	0.215147570	0.542686134
O	0.215032827	0.204772812	0.958220497
O	0.784967173	0.795227188	0.041779503
O	0.284967173	0.704772812	0.541779503
O	0.715032827	0.295227188	0.458220497

Fig. S11. Crystal lattice vectors and atomic coordinates in crystal units for relaxed structures obtained via DFT+U with a U=4eV.

References

1. Subedi A, Peil OE, Georges A (2015) Low-energy description of the metal-insulator transition in the rare-earth nickelates. *Physical Review B - Condensed Matter and Materials Physics* 91(7):1–16.
2. Seth P, et al. (2017) Renormalization of effective interactions in a negative charge transfer insulator. *Physical Review B* 96(20):205139.
3. Giannozzi P, et al. (2009) Quantum ESPRESSO: a modular and open-source software project for quantum simulations of materials. *Journal of Physics: Condensed Matter* 21:395502.
4. Mostofi AA, et al. (2014) An updated version of wannier90: A tool for obtaining maximally-localised Wannier functions. *Computer Physics Communications* 185(8):2309–2310.
5. Parcollet O, et al. (2015) TRIQS: A toolbox for research on interacting quantum systems. *Computer Physics Communications* 196(196):398–415.
6. Aichhorn M, et al. (2016) TRIQS/DFTTools: A TRIQS application for ab initio calculations of correlated materials. *Computer Physics Communications* 204:200–208.
7. Seth P, Krivenko I, Ferrero M, Parcollet O (2016) TRIQS/CTHYB: A continuous-time quantum Monte Carlo hybridisation expansion solver for quantum impurity problems. *Computer Physics Communications* 200:274–284.
8. Werner P, Millis AJ (2006) Hybridization expansion impurity solver: General formulation and application to Kondo lattice and two-orbital models. *Physical Review B - Condensed Matter and Materials Physics* 74(15):155107.
9. Vanderbilt D (1990) Soft Self-Consistent Pseudopotentials in a generalized eigenvalue formalism. *Physical review B* 41(11):7892–7895.
10. Perdew JP, Burke K, Ernzerhof M (1996) Generalized gradient approximation made simple. *Physical Review Letters* 77(18):3865–3868.
11. Peil OE, Hampel A, Ederer C, Georges A (2018) Mechanism and Control Parameters of the Metal-Insulator Transition in Nickelates. (arXiv: 1809.03720).
12. Disa AS, et al. (2017) Control of hidden ground-state order in NdNiO3 Superlattices. *Physical Review Materials* 1:024410.
13. van der Laan G (1994) Sum Rules and Fundamental Spectra of Magnetic X-Ray Dichroism in Crystal Field Symmetry. *Journal of the Physical Society of Japan* 63:2393.